Energy & Environmental Science

Hard carbon with opened pore structure for enhanced sodium storage performance

Journal:	*Energy & Environmental Science*
Manuscript ID	EE-ART-06-2024-002519.R1
Article Type:	Paper
Date Submitted by the Author:	18-Aug-2024
Complete List of Authors:	You, Shunzhang ; South China University of Technology Zhang, Qiaobao; Xiamen University, Department of Materials Science and Engineering Liu, Junxiang; Argonne National Laboratory Deng, Qiang; South China University of Technology Sun, Zhefei; Xiamen University Cao, Dandan; South China University of Technology Liu, Tongchao; Argonne National Laboratory, Chemical Science and Engineering Division Amine, Khalil; Argonne National Laboratory Yang, Chenghao; South China University, School of Environment and Energy; South China University of Technology, Key Laboratory of Fuel Cell Technology of Guangdong Province

Broader context

Hard carbons are a promising class of anode material for sodium ion batteries since they exhibit excellent initial Coulombic efficiency (ICE) and rate performance. However, the mechanisms behind such an excellent cell performance remain ambiguous. Herein, a waste wood derived hard carbon with opened pore structure (OP-HC) and enlarged interlayer spacing have been fabricated and utilized as SIB anode material. *Ex-situ* SAXS and HR-TEM testing results indicate that OP-HC with opened pores and enlarged d_{002} interlayer spacing facilitate the reversible (de)sodiation of Na^+ ions. *In-situ* TEM combined with *in-situ* XRD testing results demonstrate that OP-HC shows an excellent structure stability during the (de)sodiation process. Thus, OP-HC exhibits a high specific capacity of 350.7 mAh g^{-1} at 0.05 C, ultra-high ICE of 94.9%. Moreover, OP-HC shows an excellent cycling stability, and the assembled 18650 full cell with OP-HC anode can achieve a high capacity retention of 94.5% after 400 cycles at 1.0 A.

ARTICLE

Hard carbon with opened pore structure for enhanced sodium storage performance

Received 00th January 20xx,
Accepted 00th January 20xx

DOI: 10.1039/x0xx00000x

Shunzhang You, ‡[a] Qiaobao Zhang, ‡[b], Junxiang Liu, [c] Qiang Deng, [a] Zhefei Sun, [b] Dandan Cao, [a] Tongchao Liu, *[c] Khalil Amine *[c] and Chenghao Yang *[a]

Pore structure of hard carbon plays a great role impact on its Na^+ storage capacity. Here, a waste wood derived hard carbon with opened pores (OP-HC) has been fabricated with polyvinyl pyrrolidone (PVP) as additive. *Ex-situ* SAXS and HR-TEM testing results indicate that OP-HC with opened pores and enlarged d_{002} interlayer spacing facilitate the reversible (de)sodiation of Na^+ ions. *In-situ* TEM and XRD testing results demonstrate that OP-HC shows an excellent structure stability during the (de)sodiation process. Thus, OP-HC delivers a high reversible charge capacity is 350.7 mAh g^{-1} at 0.05 C and ultra-high initial Coulombic efficiency (ICE) of 94.9%. Moreover, OP-HC exhibits an excellent cycling stability, and the assembled 18650 full cell with OP-HC anode can achieve a high capacity retention of 94.5% after 400 cycles at 1.0 A. The excellent electrochemical performance and deep insights into OP-HC with opened pores and increased d_{002} interlayer spacing offers a new strategy to design high performance HC anode for SIBs.

Introduction

Sodium ion batteries (SIBs) have attracted great interests for their applications in low-speed electric vehicles and grid-scale energy storage systems for their excellent electrochemical performance at lower temperature, low cost and safety features.[1-4] Currently, various SIB cathode materials with competitive performance to lithium-ion batteries (LIBs) have been successfully developed.[5-8] However, the development of high performance anode materials is still a major challenge in the full-cell performance, due to the larger radius of Na^+ ions, sluggish Na^+ insertion/extraction kinetics and poor stability. To date, numerous functional materials, e.g. carbonaceous materials,[9-11] phosphides,[12, 13] oxides[14, 15] and transition metal chalcogenides (TMCs),[16, 17] etc,[18-20] have been investigated as SIBs anode materials. Among them, hard carbon with highly disordered structure and larger interlayer spacing has been considered as the promising SIB anode material for its high Na^+ storage capacity, low working potential and long cycle life.[21-23] The hard carbon derived from biomass precursors, e.g. coconut shell,[24] durian shell,[25] peanut shell,[26] and cellulose et al.,[27, 28] are active studied for their low cost and sustainability, and the obtained hard carbon materials exhibit attractive Na^+ storage capability. However, the Na^+ storage mechanism in hard carbon is still in debate, which seriously restricts the further improvement of its electrochemical performance.

Hard carbon is considered as few-layer, small, curved graphene nanosheets stacked in a disordered manner to form large granular particles with numerous defects and nanopores inside them.[29, 30] Based on the proposed Na^+ storage mechanisms in hard carbon, the crystallites, defects and nanopores directly attribute to its Na^+ storage performance.[31-33] The interlay spacing of (002) plane (d_{002}) is regarded as one of the major parameters for the crystallites that great impact its Na^+ storage capability. Theoretical calculation results indicate that d_{002} larger than 0.37 nm is kinetically favorable for Na^+ (de)intercalation.[29, 34] While, nanopores are formed among the curved graphene nanosheet during precursors carbonization process. Typically, nanopores in hard carbon particles are void and closed among the crystallites, which are isolated within the materials.[30, 35] Na^+ ions can diffuse through hard carbon, fill into the closed pores and provide Na^+ storage capacity. It is commonly accepted that Na^+ ions fill the nanopores and form quasi-metallic clusters at low-potential plateaus region, structure of the nanopores plays a vital role in the Na^+ ions filling process and determine the low-voltage plateau and average potential.[36-38] Thus, great efforts have been devoted to optimize the nanopores structure and design hard carbon anode materials with long low-voltage plateau.

Herein, a waste wood derived hard carbon with opened pores (OP-HC) has been fabricated and utilized as SIB anode material. *Ex-situ* SAXS and HR-TEM testing results indicate that OP-HC with opened pores and enlarged d_{002} interlayer spacing facilitate the reversible (de)sodiation of Na^+ ions. *In-situ* TEM combined with *in-situ* XRD testing results demonstrate that OP-HC shows an excellent structure stability during the (de)sodiation process. In comparison, some dead Na have been detected in hard carbon with closed pores (HC), and the absorption of Na^+ ions on the defective sites leads to the shrinkage of HC particles, while the filling of Na^+ ions into the

[a] *Guangzhou Key Laboratory for Surface Chemistry of Energy Materials, New Energy Research Institute, School of Environment and Energy, South China University of Technology, Guangzhou 510006, P. R. China. E-mail: esyangc@scut.edu.cn*
[b] *Department of Materials Science and Engineering, College of Materials, Xiamen University, Fujian 361005, P. R. China.*
[c] *Chemical Sciences and Engineering Division, ArgonneNational Laboratory, Lemont, IL 60439, USA. E-mail: liut@anl.gov (T.L.); amine@anl.gov (K.A.)*

† Electronic Supplementary Information (ESI) available: See DOI: 10.1039/x0xx00000x

‡ These authors contributed equally to this work.

closed pores results in the rapid expansion of HC particles. While, OP-HC exhibits a significantly improved electrochemical performance with a high reversible charge capacity is 350.7 mAh g^{-1} at 0.05 C and an ultra-high initial Coulombic efficiency (ICE) of 94.9%. Moreover, OP-HC shows an excellent cycling stability, and the assembled 18650 full cell with OP-HC anode can achieve a high capacity retention of 94.5% after 400 cycles at 1.0 A.

Results and discussion

Figure 1a and S1 schematically illustrate the preparation of OP-HC using polyvinyl pyrrolidone (PVP) as additive. For comparison, the waste wood derived hard carbon with closed pores (HC) was prepared by a similar method without adding PVP. **Figure 1b** shows the X-ray diffraction (XRD) patterns of HC and OP-HC. The XRD pattern of HC exhibits two broad peaks around 22 and 43°, corresponding to the lattice plane of (002) and (100), respectively. While, the (002) and (100) peaks of OP-HC are relative weaker, demonstrating the more disordered crystalline structure in OP-HC. Compared with HC, (002) and (100) planes of OP-HC shift towards lower 2θ, suggesting the expansion of interlayer spacing. The interlay spacing for (002) plane (d_{002}) calculated from the XRD patterns are 0.388 nm for HC and 0.414 nm for OP-HC.

Figure 1e shows the Raman spectroscopy of HC and OP-HC, both of them show the D and G peaks centered at 1354 and 1600 cm^{-1}, respectively. The intensity ratio of D to G peak (I_D/I_G) for OP-HC is 1.27, whereas I_D/I_G of HC is 1.28, indicating the similar graphitization of them.[25] Scanning electron microscope (SEM) image of HC is shown **Figure 1d**, HC exhibits a typical sawdust-like morphology with a D_{50} of 8.2 μm. While, the particles size of OP-HC is significantly reduced with a D_{50} of 5.5 μm (**Figure 1c**), it is consistent with the specific surface area and tap density testing results (**Figure S2**). Transmission Electron Microscope (TEM), Fourier transform infrared reflection (FTIR) and X-ray photoelectron spectroscopy (XPS) testing results demonstrate that the introduction of PVP does not introduce any other impurities into OP-HC (**Figure S3 and S4**). High-resolution TEM (HR-TEM) images in **Figure 1g** indicates that HC possesses a disordered structure with many closed pores. While, OP-HC displays a higher disordered structure, but the pores in OP-HC are opened up (**Figure 1f**). Moreover, OP-HC exhibits a d_{002} interlayer spacing of 0.414 nm, which is larger than that of 0.388 nm for HC.

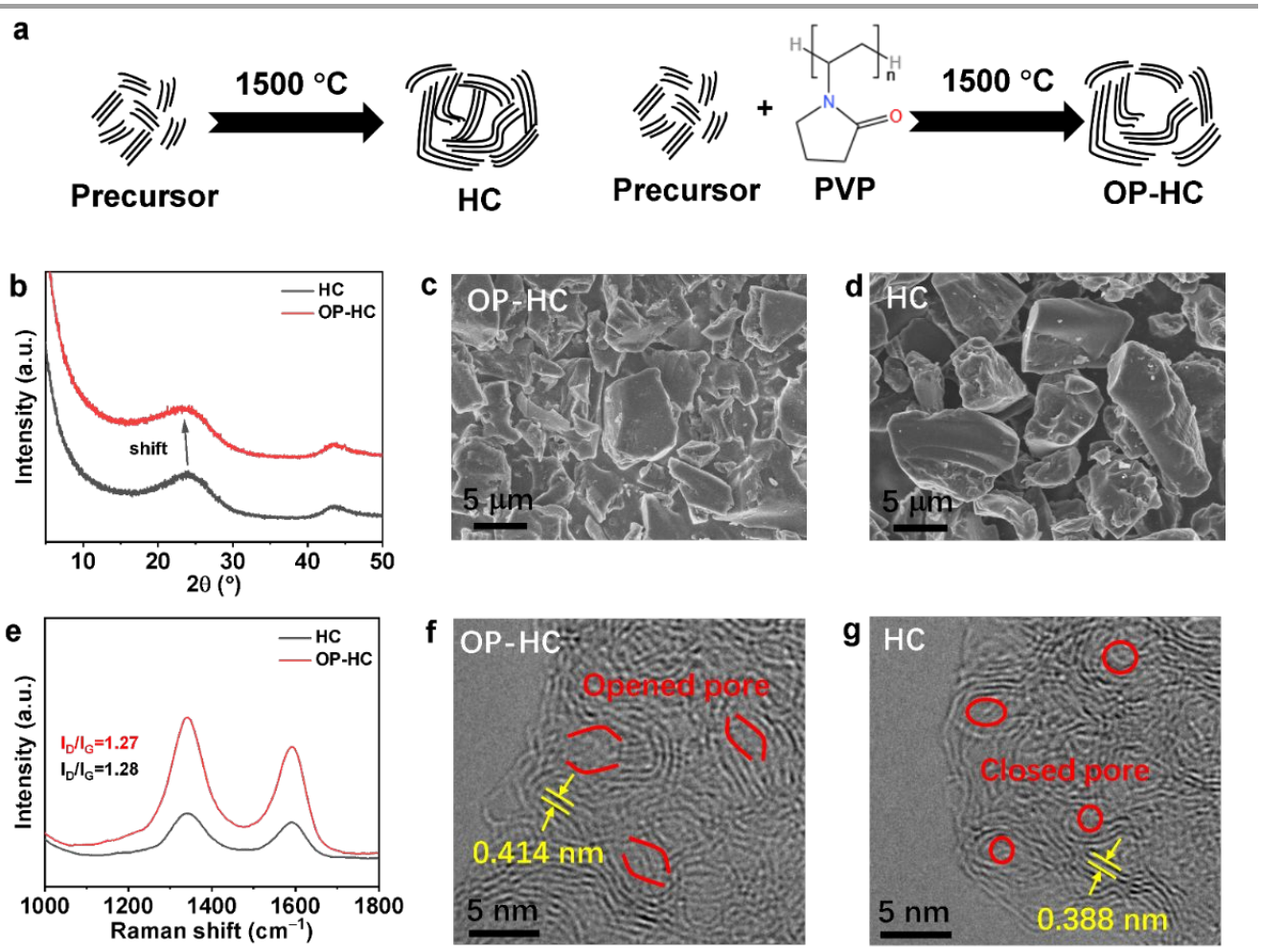

Figure 1. Schematic illustrations of the HC and OP-HC materials (a). XRD patterns (b) and Raman spectra (e) of HC and OP-HC. SEM images of OP-HC (c) and HC (d). TEM images of OP-HC (f) and HC (g).

As indicated in **Figure 2a**, OP-HC shows a high initial charge Na^+-storage capacity of 350.7 mAh g^{-1} with an ultra-high initial Coulombic efficiency (ICE) of 94.9%. But HC exhibits an initial charge capacity of only 300.7 mAh g^{-1} with an ICE of 92.8%. The high charge capacity of OP-HC is mainly ascribed to the contribution from low-voltage plateau capacity, the enlarged d_{002} interlayer spacing and opened pore structure can facilitate Na^+ ions (de)intercalation and storage (**Figure 2b**). The sodium storage performance of OP-HC synthesized under different conditions also varies (**Figure S5 and S6**). Compared with the hard carbon materials as reported elsewhere, OP-HC fabricated in this work exhibits the best comprehensive electrochemical performance in terms of excellent reversible charge capacity and the highest ICE (**Figure 2d and Table S2**). In addition, OP-HC demonstrates a high rate performance with a reversible charge capacity of 350.7, 340.2, 327.9, 312.8, 297, 261.3 and 204.8 mAh g^{-1} at 0.05, 0.1, 0.2, 0.5, 1.0, 2.0 and 3.0 C, respectively (**Figure 2c and S7a**). When the current density is set back to 0.1 C, OP-HC can still deliver a reversible charge capacity of 334.8 mAh g^{-1}. While, HC only exhibits a reversible charge capacity of 280.2, 271.5, 264.4, 250.3, 222.6, 132.3 and 64.9 mAh g^{-1} at 0.05, 0.1, 0.2, 0.5, 1.0, 2.0 and 3.0 C, respectively. Further, OP-HC exhibits a more stable cycling performance at different current densities (**Figure 2e, S7 and S8**). As shown in **Figure 2e**, OP-HC can deliver a charge capacity of 245.2 mAh g^{-1} at 1.0 C after 500 cycles, while that HC drops abruptly to almost 0 at 1.0 C after 300 cycles. Compared with the hard carbon as reported elsewhere, OP-HC exhibits distinct advantages of rate and cycling performance (**Table S3**).

Ex-situ small angle X-ray scattering (SAXS) was performed to characterize the pore structure evolution during the initial charging/discharging process. As shown in **Figure 3a**, HC shows an obvious slope between 0-3 nm^{-1}, indicating the existence of nanopores in it. When discharged 0.01 V, the slope disappears due to Na^+ ions are fully filled into the closed pores. When charged back to 2.5 V, the slop still cannot be observed because the Na^+ ions cannot be released from the closed pores smoothly, resulting in poor reversibility. Similarly, an obvious slope between 0-3 nm^{-1} can be clearly observed in the *ex-situ* SAXS curve for OP-HC, but it vanishes as discharged to 0.01 V due to the fully filling of Na^+ ions into the opened pores (**Figure 3e**). When desodiated back to 2.5 V, the slope between 0-3 nm^{-1} recovers, indicating that Na^+ ions are almost completely released from the opened pores and a high reversibility (de)sodiation process in OP-HC. This is also confirmed by the phenolphthalein reagent testing results (**Figure S9**).

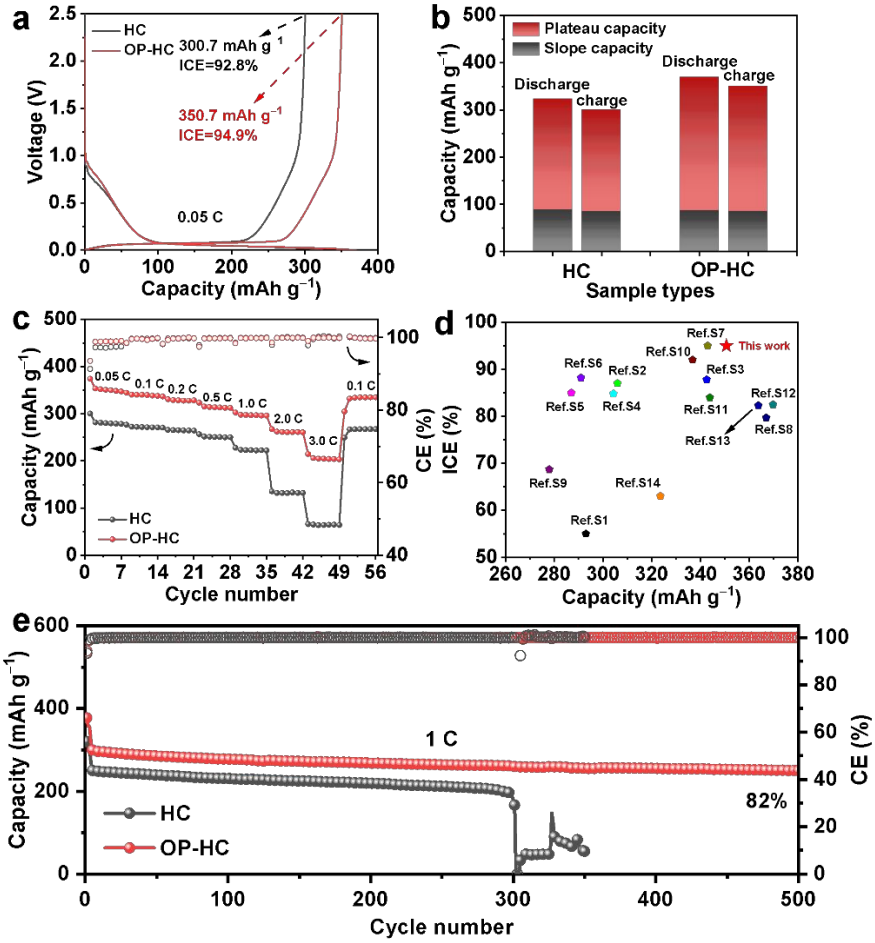

Figure 2. Charge/discharge profiles of the first cycle at 0.05 C (a) and the corresponding plateau and slope capacity (b) of HC and OP-HC. Rate performance (c) of OP-HC from 0.05 to 3.0 C. Comparison of ICE vs initial charge capacity between the OP-HC and HC anodes as reported elsewhere (d). Cycling performance of HC and OP-HC at 1.0 C (e).

Ex-situ HR-TEM testing results indicate that fresh HC is rich in closed pores with a d_{002} of 0.388 nm (**Figure 3b, 3k)**. When discharged to 0.01 V, d_{002} of HC shrinks to 0.375 nm (**Figure 3c, 3k**). As desodiation to 2.5 V, d_{002} of HC recovers slightly back to 0.376 nm (**Figure 3d, k**). But the closed pores cannot be clearly observed in **Figure 3c and d**, which is attributed to that some Na^+ ions filled in the closed pores as it is discharged to 0.01 V, but Na^+ ions adsorbed on the inner surface of the closed pores cannot be completely extracted as it is charged back to 2.5 V (**Figure 3m**). While, fresh OP-HC with opened pores exhibits a d_{002} of 0.414 nm (**Figure 3f, l**). But it shrinks to 0.403 nm when it is discharged to 0.01 V (**Figure 3g, l**), and recovers back to 0.411 nm as it is desodiated to 2.5 V (**Figure 3h, l**). It is interesting to find that, although the opened pores of OP-HC connot be clearly observed as it is sodiated to 0.01 V, the opened pores are clearly detected as it is desodiated back to 2.5 V.

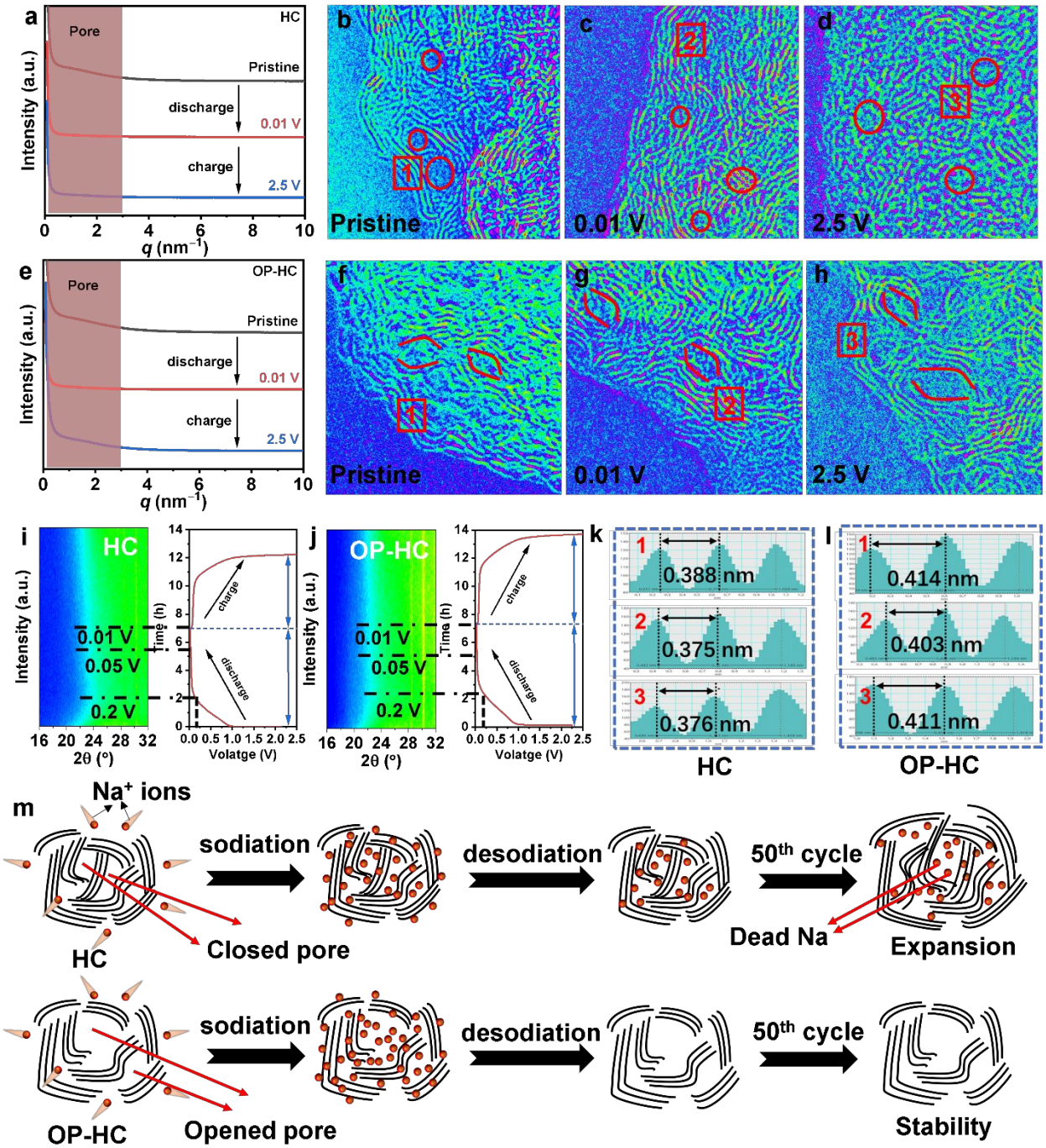

Figure 3. *Ex-situ* SAXS patterns of HC (a) and OP-HC (e) in the initial discharge/charge cycle. *Ex-situ* HRTEM of fresh (b, f), after discharged to 0.01 V (c, g), and charged to 2.5 V (d, h) and the corresponding carbon layer spacing (k, l) for HC (b-d) and OP-HC (f-h), respectively. Contour plots of *in-situ* XRD patterns (i, j) and the corresponding time-voltage curves. Schematic illustration of (de)sodiation process in HC and OP-HC (m).

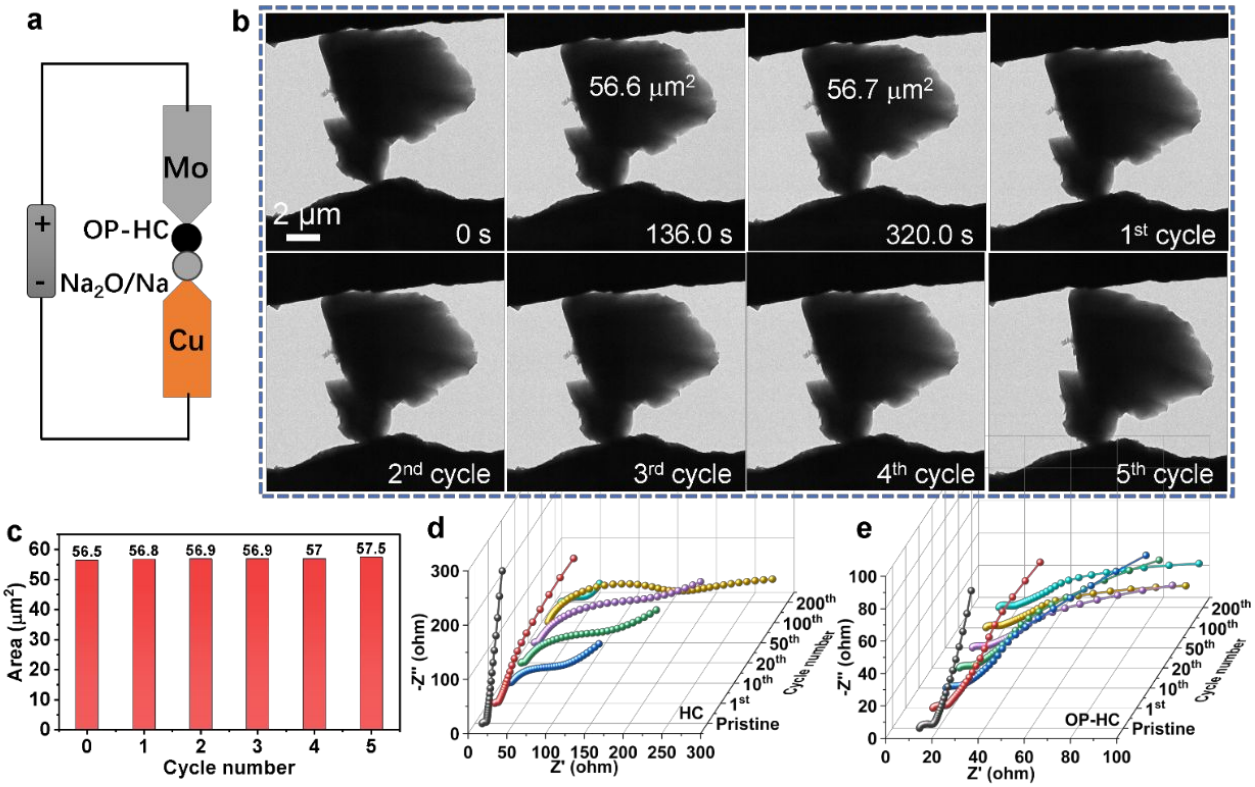

Figure 4. Schematic illustration of *in-situ* TEM apparatus (a), *in-situ* TEM images during the (de)sodiation of OP-HC (b), and the corresponding areal changes of OP-HC particles in the first five cycles (c). Operando-EIS after different cycle of (d) HC and (e) OP-HC anodes.

In-situ XRD has also further performed to understand the overall structure evolution in these two samples during the initial discharge/charge cycle under 0.1 A g^{-1} within 0.01-2.5 V on a live cell, as shown in **Figure 3i-j**. Combined with *ex-situ* SAXS and HR-TEM investigations, a three-stage Na^+-storage mechanism for OP-HC anode is schematically illustrated in **Figure 3m and S10**.[39] In stage I (OCV-0.2 V), the rapid voltage decrease associated with the (002) plane located at 22° for OP-HC shifts slight to the higher 2θ, which is attributed to its lattice shrinkage caused by Na^+ adsorption. In stage II (0.2-0.05 V), the decrease in potential associated with the (002) diffraction peak of OP-HC shifts to lower 2θ, which is ascribed to the slight lattice expansion caused by Na^+ intercalation. In stage III (0.05-0.01 V), when it is further discharged to 0.01 V, the peak of (002) plane remains stable, and it is related to the Na^+ ions filling into the open pores. During the subsequent desodiation process to 0.05 V, the peak of (002) plane keeps stable, suggesting the extraction of Na^+ ions from the opened pores. Subsequently desodiation from 0.05 to 2.5 V, the peak of (002) plane continuous shifts to the lower 2θ, demonstrating the highly reversible deintercalation and desorption of Na^+ ions from OP-HC. Similar phenomenon has been observed in the *in-situ* XRD patterns of HC (**Figure 3i**). But during the desodiation process from 2.5 to 0.05 V, the (002) diffraction peak shifts fast to higher 2θ, indicating the rapid shrinkage of (002) plane for HC. While, as it is desodiation from 0.05 to 0.01 V, the peak of (002) plane shifts fast to lower 2θ, indicating the rapid expansion of (002) plane for HC.

As shown in **Figure S10**, HC and OP-HC exhibit a similar specific capacity in the slope region of Na^+ adsorption for 67 mAh g^{-1}. During the intercalation process, the expanded (002) interlayers spacing will obviously facilitate the Na^+ intercalation, leading to an elongated plateau region of OP-HC with a high specific capacity of 160 mAh g^{-1}, which is much higher than that of HC for 148 mAh g^{-1}. During the filling process, OP-HC with opened pores structure will facilitate the Na^+ filling/extraction and correspondingly result in an increased specific capacity of 142 mAh g^{-1}, while that of HC is only 108 mAh g^{-1}. Thus, compared with HC with closed pores, the OP-HC with opened pores and expanded interlayer spacing can facilitate the Na^+ ions diffusion and effectively enhance the reversibility of (de)sodiation process, resulting a high specific capacity, ICE and enhanced cycling stability.

To further understand the excellent cycling stability of OP-HC as SIB anode, *in-situ* TEM has been conducted on a live (de)sodiation process. As exhibited in **Figure 4a**, the OP-HC anode, metallic $Na@Na_2O$ are fixed on the Mo and Cu needles as the current collector. The (de)sodiation process of OP-HC was first investigated, and the testing results are shown in **Figure 4b, c and Movie S1**. OP-HC particles have an original area of 56.5 μm^2. The area increases slightly to 56.6 μm^2 at 136 s of sodiation, as the Na^+ absorption and intercalation happens in the OP-HC particles. Further sodiation to 320 s also leads to a further slightly increase of the particles area to 56.7 μm^2, demonstrating that the Na^+ intercalation and filling into the opened pores happen in the OP-HC particles and Na^+ storage is closed to its theoretical capacity. The OP-HC particles exhibit an area of 56.8 μm^2 after the fully desodiation process, it keeps stable during cycling and exhibits an area of 56.9, 56.9, 57 and 57.5 after the fully desodiation process at 2nd, 3rd, 4th and 5th cycle, respectively (**Figure 4b, c**). While, the *in-situ* TEM testing rests for HC are shown in **Figure**

S12 and Movie S2. As indicated in the figures, the particle area of HC increases rapidly from the original 45.7 to 46.4 μm^2 after 136 s. The HC particle area increase to 47.8 μm^2 when it is further sodiated to 320 s. After fully desodiation in the first cycle, HC exhibits a dramatically increased area of 49.9 μm^2. Combined with the *in-situ* XRD testing results, it indicated that the intercalation of Na^+ ions in (002) plane of HC does not affect its volume, the rapid expansion of HC particle is mainly ascribed to the filling of Na^+ ions into the closed pores. While, the area of the HC particle increases rapidly to 52.5 and 52.9 μm^2 after fully desodiation in the 2nd and 3rd cycle, and then keeps almost stable at 52.2 and 52.6 μm^2 after fully desodiation in the 4th and 5th cycle. These findings are also verified by the sideview SEM testing results of HC and OP-HC anode films before and after 50 cycles at 0.2 C (**Figure S11**). Thus, compared with HC, the OP-HC with opened pore structure and expanded interlayer spacing shows an excellent structure stability during the (de)sodiation process.

Figure S13 shows the TEM images of HC and OP-HC after 50 cycles at 0.2 C. As indicated in the figure, thickness of the solid electrolyte interface (SEI) film for cycled HC is 5.4 nm and is uneven, while that of cycled OP-HC is 4.4 nm and is almost flat. Atomic force microscopy (AFM) was utilized to measure the roughness and mechanical properties of SEI film formed on HC and OP-HC after cycling. The SEI layer of cycled OP-HC is smoother than that of cycled HC (**Figure S14**). As exhibited in the measured force-displacement curves in **Figure S14c**, the Young's modulus of the SEI layer formed on cycled HC is found to be 1.124 GPa. In contrast, the Young's modulus of the SEI layer formed on cycled OP-HC is calculated to be 1.832 GPa, nearly 1.6 times of that for cycled HC (**Figure S14f**). Electrochemical impedance spectroscopy (EIS) was performed to study the electrode kinetics in HC and OP-HC during cycling (**Figure 4d and e**). As indicated in the figures, the Nyquist plots are consisted of a depressed semicircle in the high-frequency range corresponding to the interfacial resistance (R_{SEI}) of the SEI film and a semicircle in the medium frequency range corresponding to the charge transfer resistance (R_{ct}).[40] The impedance spectra of HC and OP-HC within the same voltage range are similar, but R_{SEI} of HC is relatively larger and increases rapidly in the initial 50 cycle during cycling (**Figure S15, S16 and Table S1**). In contrast, R_{SEI} for OP-HC is smaller and keeps almost stable during cycling. The lower and stable R_{SEI} of OP-HC/electrolyte interface is attributed to the thin, dense and stable SEI film formed on its surface.

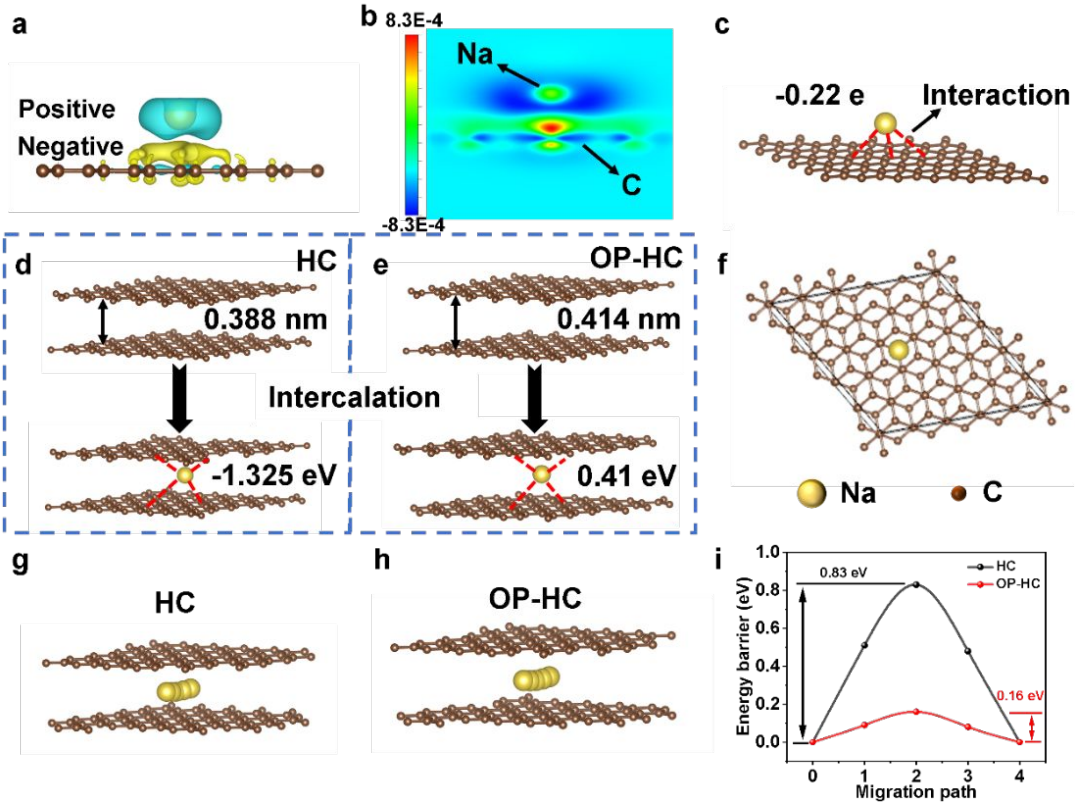

Figure 5. The different charge density (Δρ) of Na^+-graphene (a), a slice of Δρ parallels to the (010) surface (b), and the Bader charge transfer of Na^+ on graphene (c) on HC and OP-HC. Binding energy of intercalated Na^+ ion with graphene layers in HC (d) and OP-HC (e). (f) Top view of Na^+-intercalated into the graphene layers in HC and OP-HC. The migration pathway (g, h) and migration barriers (i) of Na^+ ions within the graphene layers in HC (g) and OP-HC (h), respectively.

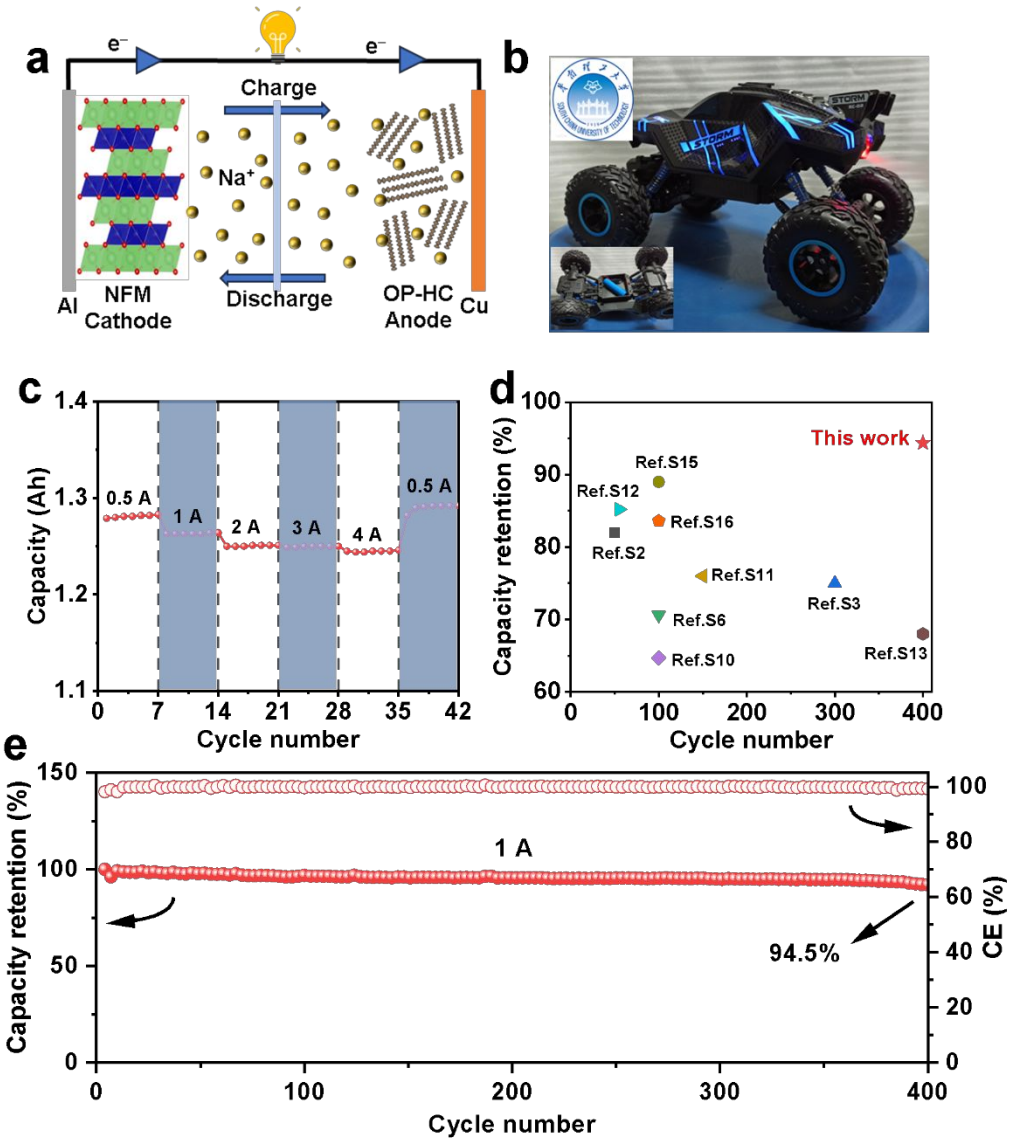

Figure 6. Schematic illustration of NFM OP-HC 18650 SIB full cell (a). Rate performance (c) for the full cell at 0.5, 1.0, 2.0, 3.0 and 4.0 A, and its application in a remote-controlled toy vehicle (b). Cycling performance of the full cell at 1.0 A (e), and comparison of the capacity retention for the full cell fabricated in this work with that of reported SIBs elsewhere (d).

Density functional theory (DFT) calculation was implemented to investigate the effect of opened pore structure and enlarged d_{002} interlayer spacing of OP-HC for Na^+-storage. As the Na^+-storage mechanism discussed above, Na^+ ions were first absorbed on HC or OP-HC surface, Na^+ ions are positively charged and carbons are negatively charged (**Figure 5a**). To figure out the electron transfer more visually, a vertical slice derived from **Figure 5a** is exhibited in **Figure 5b**. As indicated in the figures, a notable difference is observed between Na^+ and C, the charge density is mainly distributed on the C atoms. It is attributed to the oxidation of Na^+ by transferring electrons to C, and the quantity of transferred charge per Na^+ is calculated to be -0.22 e on both HC and OP-HC surface (**Figure 5c**). Thus, a quasi-ionic bond is speculated to be formed between Na^+ and C during the sodiation process.[22] To further understand the high Na^+-accommodation reversibility of in OP-HC, the intercalation of Na^+ ions into the graphene layers in HC and OP-HC were simulated, respectively, the results are exhibited in **Figure 5d-f**. It demonstrates that the deintercalation of Na^+ ions from HC is more difficult than the deintercalation of Na^+ ions from OP-HC. Thus, compared to HC, OP-HC prones to exhibit a higher reversible capacity and high ICE (**Figure 5e**). Moreover, the increased interlayer spacing has a strong influence on Na^+ ions diffusion kinetics. As indicated in **Figure 5g-i**, the Na^+ ions migration energy barrier from one hole site to the nearest hole site in these hard carbon structure decreases from 0.83 to 0.16 eV when the interlayer spacing increases from 0.388 nm of HC to 0.414 nm of OP-HC. While, the cyclic voltammetry (CV) curves at different scan rates of HC and OP-CH have also been studied (**Figure S18a, b**). The CV data of HC and OP-HC as shown in **Figure S18c and d** also support the above theoretical calculation results, and OP-HC exhibits a much higher Na^+ ions diffusion coefficient (D_{Na+})

than that of HC. The galvanostatic intermittent titration technique (GITT) results also demonstrate that OP-HC has a larger D_{Na+} than HC (**Figure S19**).

Motivated by the excellent electrochemical performance of OP-HC in half cells, 1 kg of OP-HC has been fabricated to evaluate its feasibility applications (**Figure S20a**). As illustrated in **Figure 6a and b**, the fabricated OP-HC was assembled into 18650 full cells with $NaNi_{1/3}Fe_{1/3}Mn_{1/3}O_2$ (NFM) as cathode.[41] The NFM OP-HC 18650 full cell delivers initial discharge capacities of 1.281, 1.263, 1.251, 1.249 and 1.244 Ah at 0.5, 1.0, 2.0, 3.0 and 4.0 A in the voltage range of 1.5-3.8 V at 25 °C, respectively (**Figure 6c and S20b**). When the current is set back to 0.5 A, the full cell capacity returns back to 1.291 Ah. Moreover, the full cell exhibits an average operating potential of 3.58 V and 1.239 Ah reversible capacity, resulting in a promising energy density of 150 Wh kg^{-1}. More importantly, the full cell can achieve a high capacity retention of 94.5% after 400 cycles at 1.0 A (**Figure 6e**), demonstrating an excellent cycling stability of SIB full cell ever reported (**Figure 6d and Table S4**). These excellent results indicate that OP-HC is a promising anode material for high performance SIBs.

Conclusions

In summary, a waste wood derived hard carbon with opened pores (OP-HC) and enlarged interlayer spacing has been fabricated with polyvinyl pyrrolidone (PVP) as additive. Compared to the hard carbon with closed pores (HC), OP-HC delivers a high reversible charge capacity is 350.7 mAh g^{-1} at 0.05 C and an ultra-high initial Coulombic efficiency (ICE) of 94.9%. Moreover, OP-HC exhibits an excellent cycling stability, and the assembled 18650 full cell with OP-HC anode can achieve a high capacity retention of 94.5% after 400 cycles at 1.0 A. It is attributed that the enlarged d_{002} interlayer spacing facilitates the reversible (de)intercalation and adsorption/desorption of Na^+ ions in OP-HC. However, the absorption of Na^+ ions on HC defective sites results in the shrinkage of HC particles, and the filling of Na^+ ions into the closed pores can lead to the rapid expansion of HC particles. While, OP-HC with opened pores and extended d_{002} interlayer spacing shows an excellent structure stability during cycling. The enhanced electrochemical performance on OP-HC demonstrate that this strategy will open new opportunities for developing high performance HC for SIBs.

Author Contributions

Shunzhang You: Investigation, Data curation, Writing original draft, Writing – review & editing. **Qiaobao Zhang:** Writing – review & editing. **Junxiang Liu**: Investigation, Data curation. **Qiang Deng:** Investigation, Data curation. **Zhefei Sun:** Investigation, Data curation. **Dandan Cao**: Investigation. **Tongchao Liu**: Investigation, Data curation, Writing – review & editing. **Khanlil Amine**: Investigation, Data curation, Writing – review & editing. **Chenghao Yang:** Investigation, Data curation, Writing – review & editing. All authors reviewed the manuscript.

Conflicts of interest

There are no conflicts to declare.

Acknowledgements

This work was supported by the National Key R&D Program of China (2022YFB4000120) and the Fundamental Research Funds for the Central Universities (2022ZYGXZR101).

References

1 C. Vaalma, D. Buchholz, M. Weil and S. Passerini, *Nat. Rev. Mater.*, 2018, **3**, 18013.
2 D. Saurel, B. Orayech, B. Xiao, D. Carriazo, X. Li and T. Rojo, *Adv. Energy Mater.*, 2018, **8**, 1703268.
3 S. Zhou, Z. Tang, Z. Pan, Y. Huang, L. Zhao, X. Zhang, D. Sun, Y. Tang, A. S. Dhmees and H. Wang, *SusMat*, 2022, **2**, 357-367.
4 A. Kamiyama, K. Kubota, D. Igarashi, Y. Youn, Y. Tateyama, H. Ando, K. Gotoh and S. Komaba, *Angew. Chem., Int. Ed.*, 2021, **60**, 5114-5120.
5 Y. Liu, X. Rong, R. Bai, R. Xiao, C. Xu, C. Zhang, J. Xu, W. Yin, Q. Zhang, X. Liang, Y. Lu, J. Zhao, L. Chen and Y.-S. Hu, *Nat. Energy*, 2023, **8**, 1088-1096.
6 F. Ding, C. Zhao, D. Zhou, Q. Meng, D. Xiao, Q. Zhang, Y. Niu, Y. Li, X. Rong, Y. Lu, L. Chen and Y.-S. Hu, *Energy Storage Mater.*, 2020, **30**, 420-430.
7 Z.-Y. Gu, X.-T. Wang, Y.-L. Heng, K.-Y. Zhang, H.-J. Liang, J.-L. Yang, E. H. Ang, P.-F. Wang, Y. You, F. Du and X.-L. Wu, *Sci. Bull.*, 2023, **68**, 2302-2306.
8 J.-Z. Guo, Z.-Y. Gu, M. Du, X.-X. Zhao, X.-T. Wang and X.-L. Wu, *Mater. Today*, 2023, **66**, 221-244.
9 K.-Y. Zhang, Y.-Q. Fu, H.-H. Liu, J.-L. Yang, M.-Y. Su, Y. Wang and X.-L. Wu, *Phys. Scripta*, 2023, **98**, 125977.
10 H. Wang, H. Chen, C. Chen, M. Li, Y. Xie, X. Zhang, X. Wu, Q. Zhang and C. Lu, *Chin. Chem. Lett.*, 2023, **34**, 107465.
11 C. Yang, J. Xiong, X. Ou, C.-F. Wu, X. Xiong, J.-H. Wang, K. Huang and M. Liu, *Mater. Today Energy*, 2018, **8**, 37-44.
12 Y. Lu, P. Zhou, K. Lei, Q. Zhao, Z. Tao and J. Chen, *Adv. Energy Mater.*, 2017, **7**, 1601973.
13 Z. Hu, Q. Liu, W. Lai, Q. Gu, L. Li, M. Chen, W. Wang, S.-L. Chou, Y. Liu and S.-X. Dou, *Adv. Energy Mater.*, 2020, **10**, 1903542.
14 Q. Wei, X. Chang, D. Butts, R. DeBlock, K. Lan, J. Li, D. Chao, D.-L. Peng and B. Dunn, *Nat. Commun.*, 2023, **14**, 7.
15 J. Liu, Y. Li, Z. Chen, N. Liu, L. Zheng, W. Shi and X. Wang, *J. Am. Chem. Soc.*, 2022, **144**, 23191-23197.
16 M. Yang, X. Chang, L. Wang, X. Wang, M. Gu, H. Huang, L. Tang, Y. Zhong and H. Xia, *Adv. Mater.*, 2023, **35**, 2208705.
17 M. Jiang, Y. Hu, B. Mao, Y. Wang, Z. Yang, T. Meng, X. Wang and M. Cao, *Nat. Commun.*, 2022, **13**, 5588.
18 B. Li, B. Xi, Z. Feng, Y. Lin, J. Liu, J. Feng, Y. Qian and S. Xiong, *Adv. Mater.*, 2018, **30**, 1705788.
19 Y. Liang, N. Song, Z. Zhang, W. Chen, J. Feng, B. Xi and S. Xiong, *Adv. Mater.*, 2022, **34**, 2202673.
20 H. Shen, Y. An, Q. Man, D. Liu, X. Zhang, Z. Ni, Y. Dai, M. Dong, S. Xiong and J. Feng, *Adv. Funct. Mater.*, 2024, **34**, 2309834.
21 Y. Qi, Y. Lu, F. Ding, Q. Zhang, H. Li, X. Huang, L. Chen and Y.-S. Hu, *Angew. Chem., Int. Ed.*, 2019, **58**, 4361-4365.

22 Z. Wang, X. Feng, Y. Bai, H. Yang, R. Dong, X. Wang, H. Xu, Q. Wang, H. Li, H. Gao and C. Wu, *Adv. Energy Mater.*, 2021, **11**, 2003854.

23 H. Au, H. Alptekin, A. C. S. Jensen, E. Olsson, C. A. O'Keefe, T. Smith, M. Crespo-Ribadeneyra, T. F. Headen, C. P. Grey, Q. Cai, A. J. Drew and M.-M. Titirici, *Energy Environ. Sci.*, 2020, **13**, 3469-3479.

24 C. Nita, B. Zhang, J. Dentzer and C. Matei Ghimbeu, *J. Energy Chem.*, 2021, **58**, 207-218.

25 S. You, Q. Deng, Q. Zhang, K. Huang and C. Yang, *ACS Sustain. Chem. Eng.*, 2023, **11**, 10590-10597.

26 W. Lv, F. Wen, J. Xiang, J. Zhao, L. Li, L. Wang, Z. Liu and Y. Tian, *Electrochim. Acta*, 2015, **176**, 533-541.

27 H. Yamamoto, S. Muratsubaki, K. Kubota, M. Fukunishi, H. Watanabe, J. Kim and S. Komaba, *J. Mater. Chem. A*, 2018, **6**, 16844-16848.

28 H. Yang, R. Xu and Y. Yu, *Energy Storage Mater.*, 2019, **22**, 105-112.

29 L.-F. Zhao, Z. Hu, W.-H. Lai, Y. Tao, J. Peng, Z.-C. Miao, Y.-X. Wang, S.-L. Chou, H.-K. Liu and S.-X. Dou, *Adv. Energy Mater.*, 2021, **11**, 2002704.

30 N. Sun, J. Qiu and B. Xu, *Adv. Energy Mater.*, 2022, **12**, 2200715.

31 Y. Jin, S. Sun, M. Ou, Y. Liu, C. Fan, X. Sun, J. Peng, Y. Li, Y. Qiu, P. Wei, Z. Deng, Y. Xu, J. Han and Y. Huang, *ACS Appl. Energy Mater.*, 2018, **1**, 2295-2305.

32 X. Chen, J. Tian, P. Li, Y. Fang, Y. Fang, X. Liang, J. Feng, J. Dong, X. Ai, H. Yang and Y. Cao, *Adv. Energy Mater.*, 2022, **12**, 2200886.

33 J. Zhao, X.-X. He, W.-H. Lai, Z. Yang, X.-H. Liu, L. Li, Y. Qiao, Y. Xiao, L. Li, X. Wu and S.-L. Chou, *Adv. Energy Mater.*, 2023, **13**, 2300444.

34 S. Alvin, H. S. Cahyadi, J. Hwang, W. Chang, S. K. Kwak and J. Kim, *Adv. Energy Mater.*, 2020, **10**, 2000283.

35 L. Kitsu Iglesias, E. N. Antonio, T. D. Martinez, L. Zhang, Z. Zhuo, S. J. Weigand, J. Guo and M. F. Toney, *Adv. Energy Mater.*, 2023, **13**, 2302171.

36 Y. Chu, J. Zhang, Y. Zhang, Q. Li, Y. Jia, X. Dong, J. Xiao, Y. Tao and Q.-H. Yang, *Adv. Mater.*, 2023, **35**, 2212186.

37 N. LeGe, X.-X. He, Y.-X. Wang, Y. Lei, Y.-X. Yang, J.-T. Xu, M. Liu, X. Wu, W.-H. Lai and S.-L. Chou, *Energy Environ. Sci.*, 2023, **16**, 5688-5720.

38 G. Liu, Z. Wang, H. Yuan, C. Yan, R. Hao, F. Zhang, W. Luo, H. Wang, Y. Cao, S. Gu, C. Zeng, Y. Li, Z. Wang, N. Qin, G. Luo and Z. Lu, *Adv. Sci.*, 2023, **10**, 2305414.

39 C. Bommier, T. W. Surta, M. Dolgos and X. Ji, *Nano Lett.*, 2015, **15**, 5888-5892.

40 R. Dong, L. Zheng, Y. Bai, Q. Ni, Y. Li, F. Wu, H. Ren and C. Wu, *Adv. Mater.*, 2021, **33**, 2008810.

41 N. Hong, J. Li, S. Guo, H. Han, H. Wang, X. Hu, J. Huang, B. Zhang, F. Hua, B. Song, N. Bugday, S. Yasar, S. Altin, W. Deng, G. Zou, H. Hou, Z. Long and X. Ji, *J. Mater. Chem. A*, 2023, **11**, 18872-18880.

The data supporting this article have been included as part of the Supplementary Information.